Theoretical and Applied Fracture Mechanics 101 (2019) 80–91

Contents lists available at ScienceDirect

Theoretical and Applied Fracture Mechanics

journal homepage: www.elsevier.com/locate/tafmec

On the estimation of the elastoplastic work needed to initiate crack tearing

Luiz Fernando Nazaré Marques[a,*], Eduardo Enes Cota[b], Jaime Tupiassú Pinho de Castro[b], Luiz Fernando Martha[b], Marco Antonio Meggiolaro[b]

[a] Federal University of South and Southeast of Pará, UNIFESSPA, Avenida dos Ipês s/n, Marabá, 68500-000, Brazil
[b] Pontifical Catholic University of Rio de Janeiro, PUC-Rio, Rua Marquês de São Vicente 225, Rio de Janeiro 22451-900, Brazil

ARTICLE INFO

Keywords:
3D finite elements
Incremental elastoplastic calculations
3D plastic zone estimates
Elastoplastic work
Toughness estimates

ABSTRACT

Plastic zones (*pz*) ahead of crack tips are obtained by incremental elastoplastic (EP) finite element (FE) 3D calculations for cracked components with relatively high and low transversal constraints, considering all effects associated with their geometry and loading conditions. Contrary to what is assumed in traditional Fracture Mechanics estimates, *pz* sizes and shapes do not depend only on the given crack driving force K or J. They depend as well on usually neglected geometric and load parameters such as the component width-to-thickness W/B, the crack size-to-component width a/W, and in particular the nominal stress-to-yield strength σ_n/S_Y ratios. Since damage ahead of the crack front depends on the plastic work spent inside the *pz*, this fact can have a major importance in practical applications, including in fatigue and in EP fracture estimates. This work proposes a methodology for evaluating *pz* volumes based on a sub-modeling FE analysis that uses the influence volume around a plastified Gauss integration point, instead of the entire plastified FE. This technique is then used to estimate the resistance to crack tearing initiation, assuming it can be obtained from the EP work spent inside the *pz*. Such estimates are validated using the ratio of experimental fracture toughness at the threshold of crack tearing for different W/B, a/W, and σ_n/S_Y combinations.

1. Introduction

It is a truism to say that stress/strain fields around crack tips are most important in structural integrity evaluations, since they are the actual cause for failure mechanisms such as fatigue crack growth (FCG), stable tearing, and unstable fracture. However, in spite of their major practical importance, traditional plastic zone (*pz*) estimates and thus structural integrity evaluations based on them, can be highly inaccurate.

Crack driving forces usually are indirectly quantified by stress intensity factors (SIFs) K or by J-integral J, their equivalent energy release rates ($J = K^2/E$ in plane stress under linear elastic (LE) Fracture Mechanics conditions, where E is Young's modulus). SIFs can be used, for instance, to predict brittle fractures in mode I by comparing applied K_I values with a plane strain fracture toughness, K_{IC}, assumed a material property if the *pz*s, that always form ahead of crack tips, are small compared to the cracked component geometry. Indeed, it is well known that ASTM E399 standard procedures for measuring K_{IC} require $\{a, W, (W - a)$, and $B\} > 2.5 \cdot (K_{IC}/S_Y)^2$ [1], where a is the crack size, W is the cracked component width, B is the its thickness, $(W - a)$ is its residual ligament, and S_Y is the yield strength of the material. However, E399 standard procedures also specify that K_{IC} must be measured maintaining the crack size in a small $0.45 < a/W < 0.55$ range, a strange requirement for a mechanical property, to say the least. In fact, if fracture predictions must be valid for any crack in relatively brittle components, how come K_{IC} must be measured in such a limited a/W range?

Moreover, fracture predictions become even less reliable when the *pz* sizes are not so small and J should be used instead of K to quantify the crack driving forces. Indeed, the fracture toughness of cracked components (made of a same material) can vary a lot both with their geometry and with their loading conditions in such cases [2]. Maybe for this reason, there are still too many standards for toughness measurements that allow *pz*s much larger than E399 requirements, but not even the newer like the ASTM E1820 [3], whose purpose is to unify toughness measurement procedures, solve this problem. Even though the present standard procedures for elastoplastic (EP) toughness measurements are understandably conservative, it is well-known that they do yield too conservative fracture predictions in many design cases. In fact, fracture toughness is not even a material property in most practical

* Corresponding author.
E-mail addresses: lfernando@unifesspa.edu.br (L.F.N. Marques), eduardo7Cota@hotmail.com (E.E. Cota), jtcastro@puc-rio.br (J.T.P.d. Castro), lfm@tecgraf.puc-rio.br (L.F. Martha), meggi@puc-rio.br (M.A. Meggiolaro).

https://doi.org/10.1016/j.tafmec.2019.02.007
Received 16 December 2018; Received in revised form 8 February 2019; Accepted 12 February 2019
Available online 14 February 2019
0167-8442/

Nomenclature

a	crack length
A_2	constraint parameter
B	specimen thickness
B_N	specimen net thickness
C(T)	compact tension specimen
COD	crack opening displacement
CTOD	crack tip opening displacement
DIC	digital image correlation
E	Young's modulus of elasticity
EP	elastoplastic
E_s	element size
$f(a/W)$	geometry function
FCG	fatigue crack growth
FE	finite element
H	monotonic Ramberg-Osgood hardening coefficient or half-height
h	monotonic Ramberg-Osgood hardening exponent
I_2	second invariant of the deviatoric stresses
J	J-integral (energy release rate of EP materials)
J_{IC}	plane strain fracture toughness characterized by J
k	yield limit in simple shear
K, K_I	stress intensity factor (SIF) in mode I
K_{IC}	plane strain fracture toughness
L	half- length
LE	linear elastic
LLD	load-line displacement
mp	middle position
M(T)	middle tension specimen
P	load
P_{IC}	critical load used to determine J_{IC}
pl, PL	plastic
pl-ε	plane strain
pl-σ	plane stress
P_{min}, P_{max}	minimum and maximum load
pz	plastic zone
Q	triaxial stress parameter
R	load ratio (P_{max}/P_{min})
r_{pz}	plastic zone radius
SE(B)	single edge bend specimen
SE(T)	single edge tension specimen
s_1, s_2, s_3	deviatoric stress components
SIF	stress concentration factor
s_x, s_y, s_z	normal deviatoric stresses
S_Y	yield strength
T-stress	second term of elastic crack-tip stress field
T_z	triaxial stress constraint
$u(x)$	horizontal displacement
U_{EP}	elastoplastic work
u_{ep}	elastoplastic work density
U_{PL}	plastic work
$v(y)$	vertical displacement
V_a	analytical PL volume
V_e	volume of the element
V_n	numerical PL volume
V_t	total volume
W	specimen width
w	deflection
$w(z)$	out-of-plane displacement
w_0	central deflection
w_0^*	central deflection when the yield stress is reached
x, y, z	global Cartesian coordinates
ν	Poisson's coefficient
σ_n	nominal stress
δ_{IC}	critical crack tip opening displacement
ε_{eq}	Mises equivalent strain
ε_Y	yield strain
Δa	crack extension between the compliance points
α	V-notch angle
ρ	parameter for which the yield limit is reached or V-notch root radius
σ_x, σ_y, σ_z	normal stresses
τ_{xy}, τ_{xz}, τ_{yz}	shear stresses

applications. Since it is difficult if not practically impossible to estimate reliably how much conservative such predictions are in practice, fracture predictions remain far less precise than the no-fracture ones.

$K + T$-stresses, the second term of William's LE crack-tip stress fields, can partially explain toughness variations. Likewise, Q or A_2 constraint factors can be combined with J in two-parameter EP toughness estimates. A third parameter T_z can help to better model them [4–13]. However, K and J-based stress/strain fields are singular at the crack tip and tend to zero far from it, not to the nominal stress/strain values as they should. Hence, they do not properly reflect the most important σ_n/S_Y effect on the *pz* sizes, as studied elsewhere [14]. Thus, it is worth to calculate directly the three-dimensional (3D) *pz* volumes induced by a given K or J around the crack tip and then the plastic work U_{PL} dissipated inside them, instead of insisting on trying to find a single fracture toughness parameter based on K, J, or on K-T, J-Q, J-A_2, K-T-T_z, or J-Q-T_z [15] combinations. Such calculations may require non-trivial numerical techniques, but this is not a major barrier anymore.

Indeed, from a physical point of view, it is at least reasonable to assume that the toughness of most metallic cracked structural components depends primarily on the U_{PL} spent inside the *pz*. Such a hypothesis should be valid when they are tough enough to make the work spent in creating new crack faces during crack tearing much smaller than the plastic work spent in such cases. Indeed, glasses and Al alloys have similar Young's modulus, thus should need similar energies to create new crack faces. However, while the toughness of glasses is on the order of 10 J/m^2, for the tougher Al alloys it is on the order of 100 kJ/m^2. Since reliable U_{PL} calculations can already be performed in many commercial finite element (FE) codes nowadays, there is no good reason to avoid them in practical applications anymore. Moreover, toughness variation predictions based on the U_{PL} calculated inside *pz*s are experimentally verifiable by relatively simple crack tearing initiation measurements in different components made of the same material.

However, it would be naive to assume that reliable incremental 3D EP FE *pz* calculations for real cracked components are simple tasks, or that fracture toughness is a mechanical property, for that matter. It usually is not, so it cannot be assumed or treated as if it was. In most practical cases, it depends on the material and on several characteristics of the cracked component geometry too, as well as on its loading conditions. Moreover, the saying "good predictions cannot be expected from overly simplified models" is particularly true for the U_{PL} estimates inside *pz*s around crack tips. Good calculations must properly consider all effects associated with the actual cracked component geometry and loading conditions, including incremental crack tip blunting and load redistribution at each load step. They must consider as well the actual material properties.

There is a number of detailed 3D numerical studies to characterize *pz* developed around crack fronts and to quantify their effects on the structural integrity of cracked mechanical components, see for instance [16–18]. However, to the authors' knowledge, they do not correlate the plastic work spent inside them with the component toughness, the main goal of this work.

It is not a surprise that ductile materials are tough, since they dissipate more U_{PL} while plastically deforming in tensile tests than the brittle ones (albeitin tensile tests plastic work may involve cavitation and void coalescence, whereas in fracture toughness tests it involves *pz* formation and gradual crack tearing). Hence, the fracture resistance depends on geometric parameters, loading conditions, and transversal constraints, which much affect *pz* sizes and shapes, thus the U_{PL} spent inside the *pz*. Recent contributions in this subject can be found e.g. in [19–22]. However, all such papers adopt the classic approach based on *K* or *J* and/or on its combinations with constraint factors. Yet, this large amount of work contributes to quantify and to evaluate the crack front constraints. For instance, an explicit expression to quantify constraint losses is proposed in [19]. Theoretical and 3D numerical studies based on the J-A_2 EP two-parameter Fracture Mechanics approach for different geometries and thicknesses are presented in [20]. A new equation for plastic factors that considers geometric characteristics and material hardening is proposed in [21,22].

To validate the methodology proposed and used in this work, first its 3D EP FE procedures are used to generate numerical predictions that can be compared with analytical solutions for an un-cracked structural beam. Then, the proposed 3D EP sub-modeling FE predictions are compared with numerical analyses and experimental data recently published for some cracked specimens. In the sequence, their numerical predictions for *pz* sizes and shapes are compared with some 3D Digital Image Correlation (DIC) measurements made on the surface of cracked specimens.

After validating the proposed modeling techniques, they are used to calculate *pz* sizes and shapes, as well as the U_{PL} dissipated inside them. Cracked components with various a/W and σ_n/S_Y ratios under both high and low transversal displacement constraints around the crack front are considered. Finally, the U_{PL} dissipated inside the *pz*s under such different conditions are calculated and compared with some fracture toughness data measured at the crack tearing initiation threshold. In a few graphs U_{EP} is plotted instead of U_{PL} to allow direct comparisons with literature results, but the difference between them is small in tough materials. The following sections study in details all such steps.

2. Three-dimensional plastic zone analyses

Unlike assumed in traditional Fracture Mechanics estimates, *pz* sizes, shapes, and volumes can vary a lot for a given nominal driving force *K* or *J* [14]. Since both the material toughness and its resistance to fatigue crack growth depend on the EP work spent inside the *pz*, neglecting this fact can have a major importance in fracture and fatigue assessments. To support this claim, a series of EP FE 3D calculations are used to estimate *pz* sizes and shapes induced by constant SIFs K_I in various components with different loading conditions and geometric parameters. To do so, several nominal stress-to-yield strength ratios σ_n/S_Y are simulated at various crack length-to-specimen width a/W and specimen width-to-specimen thickness W/B ratios. It is well known that a same K_I can induce different *pz* sizes and shapes in thin or thick components (associated with predominantly plane stress or plane strain conditions along the crack front), because transversal displacement constraints dependent on the cracked component thickness *B* can much restrict plastic deformations. However, equally important nominal load and crack size effects, dependent on σ_n/S_Y and a/W ratios, are simply neglected in traditional *pz* estimates.

For each cracked component geometry simulated in this work, first a 3D EP global FE model is generated and meshed using properly refined elements around the crack front, gradually increasing their size in regions away from it to limit the models' size without compromising their numerical accuracy. M(T), C(T), SE(T), and SE(B) specimens are simulated in such a way in this study. A sub-model is then generated using the global model solution as new contour conditions, to improve the numerical predictions accuracy. The *pz* EP frontiers, in terms of the equivalent Mises strain, are remapped to ensure that the total volume of the *pz* is entirely within the sub-model with fine meshes of uniform element size for the final solution, as illustrated in Fig. 1.

The properties of the materials used in all simulations are presented in Table 1, where *E* is Young's modulus, ν is Poisson's coefficient, S_Y is yielding strength, while *H* and *h* are the monotonic Ramberg-Osgood strain hardening coefficient and exponent.

Both aluminum alloys are used to validate the model based on results taken from the literature [16–18]. The 2024-T3 Al is used to estimate *pz* sizes, shapes and U_{PL} in highly-constrained C(T) and lightly-constrained SE(T) specimens. There are standard K_I expressions for all specimens analyzed in this study, where $K_I = [P/\sqrt{(B \cdot B_N \cdot W)}] \cdot f(a/W)_{Specimen}$, B_N is the net thickness due to eventual side grooves and $f(a/W)_{Specimen}$ is a geometry function that depends on the crack size-to-specimen width a/W ratio. These functions for the M(T), C(T), SE(T), and SE(B) specimens are given by:

$$f\left(\frac{a}{W}\right)_{M(T)} = \sqrt{\left(\frac{\pi a}{4W}\right)\sec\left(\frac{\pi a}{2W}\right)}\left[1 - 0.025\left(\frac{a}{W}\right)^2 + 0.06\left(\frac{a}{W}\right)^4\right] \quad (1)$$

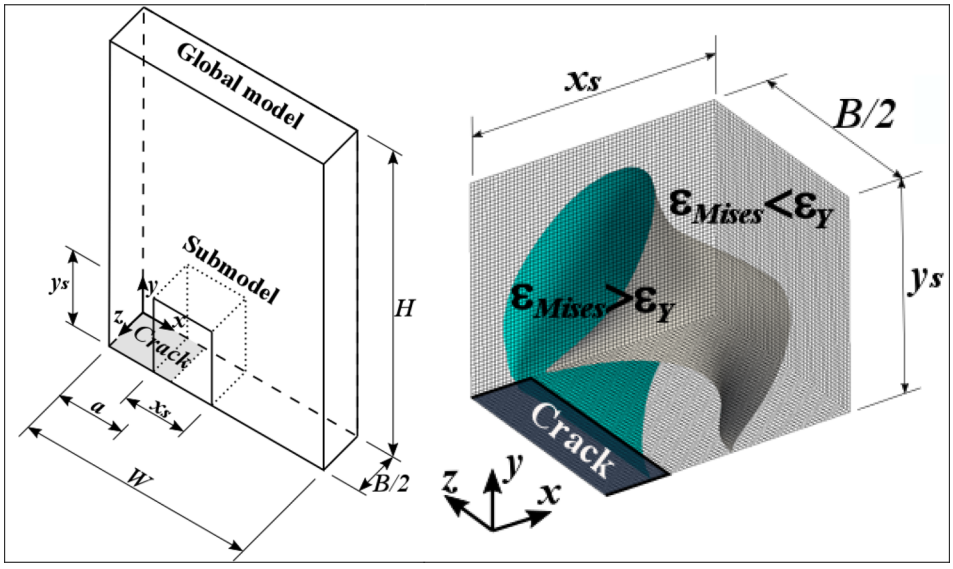

Fig. 1. Some characteristics of the global models and sub-models.

Table 1
Materials and properties.

Material	E (GPa)	ν (–)	S_Y (MPa)	H (MPa)	h (–)
2024-T3	73.1	0.33	345	–	–
2024-T351	73.5	0.33	425	685	0.073

$$f\left(\frac{a}{W}\right)_{C(T)} = \frac{(2 + a/W)}{(1 - a/W)^{3/2}}\left[0.886 + 4.64\left(\frac{a}{W}\right) - 13.32\left(\frac{a}{W}\right)^2 + 14.72\left(\frac{a}{W}\right)^3 - 5.6\left(\frac{a}{W}\right)^4\right] \quad (2)$$

$$f\left(\frac{a}{W}\right)_{SE(T)} = \frac{\sqrt{2\tan(\pi a/2W)}}{\cos(\pi a/2W)}\left[0.752 + 2.02\left(\frac{a}{W}\right) + 0.37\left(1 - \sin\frac{\pi a}{2W}\right)^3\right] \quad (3)$$

$$f\left(\frac{a}{W}\right)_{SE(B)} = \frac{3\left(\frac{a}{W}\right)^{1/2}\left[1.99 - \left(\frac{a}{W}\right)\left(1 - \frac{a}{W}\right)\left(2.15 - 3.93\left(\frac{a}{W}\right) + 2.7\left(\frac{a}{W}\right)^2\right)\right]}{2\left(1 + 2\frac{a}{W}\right)\left(1 - \frac{a}{W}\right)^{3/2}} \quad (4)$$

The SE(B) specimen geometry is shown in Fig. 2. The three other geometries can be found e.g. in the ASTM standards mentioned above.

3. FE validation and verification

All validations of the 3D EP FE models and sub-models developed in this work involve direct comparisons with numerical results or with suitable experimental data published in the literature. First, the model predictions are compared with a classic analytical solution for an un-cracked simply supported EP prismatic beam, proposed by Prager and Hodgea long time ago [23]. Then, the results of our analyses for two standard cracked specimens are compared with similar numerical results found in the literature [16–18]. These references also present an experimental validation for their *pz* sizes, performed by measuring displacements on the surface of the specimens using Digital Image Correlation (DIC) techniques. DIC is used as well to verify experimentally some numerical results obtained in this work. For these simulations, mesh convergence was tested prior to the simulations, to establish the mesh refinement parameters needed for all of them.

3.1. Analytical EP solution for a beam loaded uniformly

The initial verification of the numerical calculations involves the un-cracked, simply supported prismatic beam with rectangular cross section illustrated in Fig. 3. This beam carries a uniformly distributed load P in the y-axis direction. This problem has an analytical solution presented by Prager and Hodge [23], which isused here to validate an initial simple 3D EP FE model.

The Ansys software is used for these numerical experiments. The main objective of this section is to calculate numerically the fraction of the 3D plastic zone generated inside the EP beam by a given applied distributed load.

Usually, the smallest unit of volume considered in EP numerical simulations is the volume of the finite element V_e used in the modeling. In spite of the reasonable agreement between experimental data and its numerical predictions claimed in the literature [16], the criterion to select the smallest unit considered in the plastic regions can be improved. The V_e method adds the entire element volume to the *pz* volume, even when only one of its Gauss integration points is plastified ($\varepsilon_{eq} \geq \varepsilon_Y$) at the *EP* frontier of the *pz*. Hence, this calculation method can lead to different *pz* volumes depending on the type of elements and meshes.

For this reason, both element type and mesh convergence studies were performed here based on evaluations of the total volume, *Vt*, of the *pz* developed inside the beam when it is loaded. Linear and quadratic elements are used for these 3D EP FE simulations, and only the fractions of the volumes corresponding to their plastified Gauss integration points are counted as part of the plastified regions. Thus, the smallest volume unit for the *pz* models is $V_e/8$ in this approach. All numerical simulations are performed considering only 1/4 of the modeled beam due to its symmetries, using $L = 300$ mm, $L/B = 10$, $B/H = 1$, $E = 210$GPa, $S_Y = 300$ MPa, $\nu = 0.3$, $P_0 = 4BS_Y$, and $\rho = (P/P_0)(L/H)^2$. P is the uniformly applied load, ρ defines the percentage of the cross section plastification and $2L$, $2B$ and $2H$ are the beam length, thickness and height, respectively. Fig. 4 shows the constraint sused in this model. The commented Ansys Parametric Design Language (APDL) macro used to solve this problem is presented in Appendix A.

The verification involves numerical simulations using both V_e and $V_e/8$ criteria. Two types of FE are used to model the beam, 3D SOLID185 linear elements with 8 nodes each and 3D SOLID186 quadratic elements with 20 nodes each, both with 8 integration points per

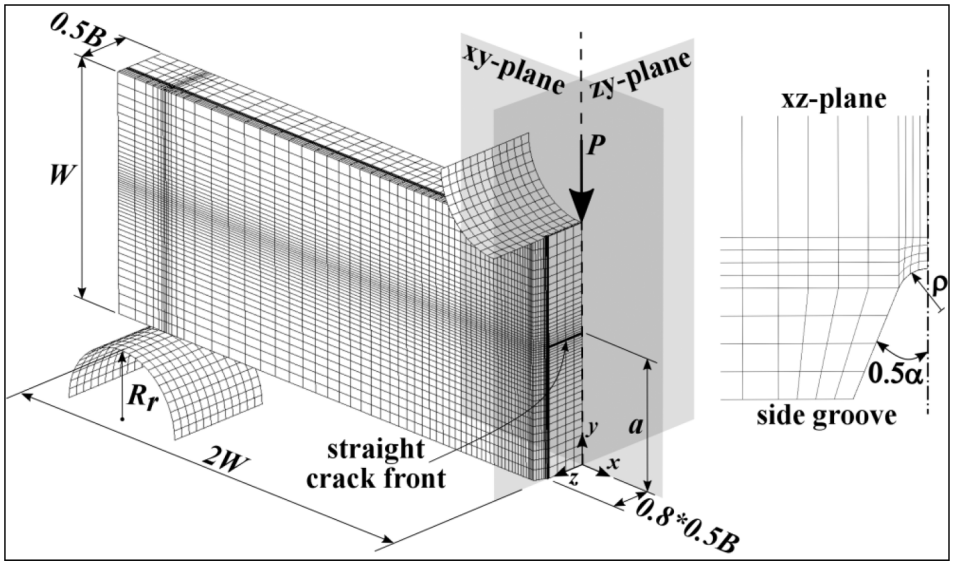

Fig. 2. SE(B) specimen geometry and side groove detail.

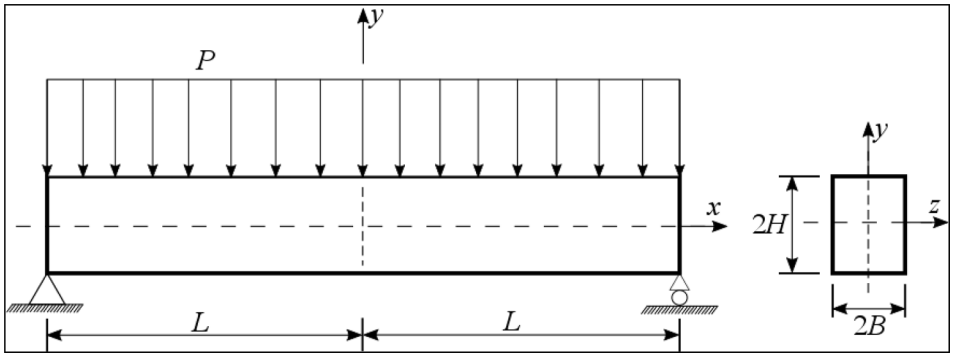

Fig. 3. Simply supported prismatic EP beam under uniform transversal load.

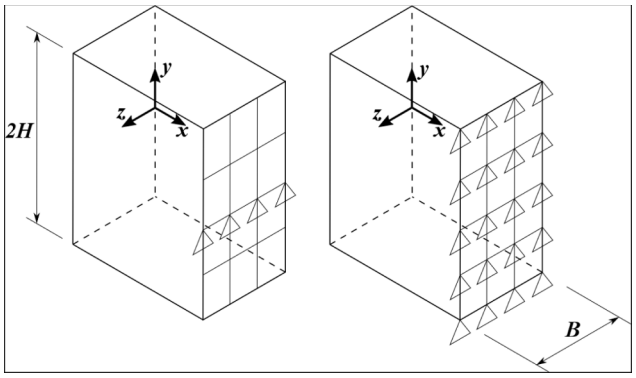

Fig. 4. The two constraints used in the EP beam model.

element and 3 degrees of freedom per node. The classic beam theory assumes plane stress conditions, so $\sigma_z = \sigma_y = \tau_{yz} = \tau_{xz} = 0$. Therefore, it can use simpler notations, $\sigma_x = \sigma$ and $\tau_{xy} = \tau$. In addition, the deviatoric components of the stress tensor are $s_x = 2\sigma/3$, $s_y = -\sigma/3$, $s_z = -\sigma/3$, $\tau_{xy} = \tau$, $\tau_{xz} = \tau_{yz} = 0$. The Mises yield condition, defined by $I_2 - k^2 = 0$, then becomes:

$$\sigma^2 + 3\tau^2 = 3k^2 \tag{5}$$

where the constant k is the yield limit in simple shear and I_2 is the second invariant of the deviatoric stresses s_i, $I_2 = (s_1^2 + s_2^2 + s_3^2)/2 = (s_x^2 + s_y^2 + s_z^2)/2 + \tau_{xy}^2 + \tau_{xz}^2 + \tau_{yz}^2$.

Assuming that the shear stress is smaller than the bending stress, the deflection $w = w(x)$ of the beam is small compared to its cross-section dimensions, and its cross sections remain planar under bending and normal to its axis when deformed, then Eq. (5) reduces to Eq. (6) and the axial strain in the beam is given by Eq. (7):

$$|\sigma| = k\sqrt{3} \tag{6}$$

$$\varepsilon_x = -y\frac{d^2w}{dx^2} \tag{7}$$

Using Hooke's law, the stress is calculated by Eq. (8) at all elastic points:

$$\sigma = -Ey\frac{d^2w}{dx^2} \tag{8}$$

Eq. (8) shows σ as an odd function of y. In any cross section along the x-axis, the yield stress is reached simultaneously for $y = \pm H$, and the plastic domains will spread from the top and bottom of the cross section. Within these plastic domains given by Eq. (9), the plus sign applies to the plastic region bordering that elastic region where σ calculated by Eq. (8) is positive:

$$\sigma = \pm k\sqrt{3} \tag{9}$$

In the EP frontier domains, $y = \pm \zeta(x)$, $(0 < \zeta \leq H)$. Since σ must be a continuous function of y, it follows from Eqs. (8) and (9) that σ can be calculated at a cross section which is partly elastic and partly plastic:

$$\begin{cases} \sigma = -k\sqrt{3} & \text{for } -H \leqslant y \leqslant -\zeta \\ \sigma = \frac{ky\sqrt{3}}{\zeta} & \text{for } -\zeta \leqslant y \leqslant \zeta \\ \sigma = k\sqrt{3} & \text{for } \zeta \leqslant y \leqslant H \end{cases} \tag{10}$$

The bending moment due to a stress σ at a generic cross section along the x-axis is given by:

$$M(x) = 4B\int_0^H \sigma(x,y)y\ dy \tag{11}$$

Substituting Eq. (8)–(10) into (11) and integrating, then:

$$\begin{cases} \mathrm{M(x)} = -\frac{4}{3}EBH^3\frac{d^2w}{dx^2} & \text{for entirely elastic cross section} \\ \mathrm{M(x)} = 2\sqrt{3}BkH^2 & \text{for entirely plastic cross section} \\ \mathrm{M(x)} = \frac{2}{3}\sqrt{3}kB(3H^2 - \zeta^2) & \text{for elastic - plastic cross section} \end{cases} \tag{12}$$

The bending moments due to internal stresses and to the external load must be equated to obtain $y = \zeta(x)$. For this case, the bending moment caused by the load P is:

$$M(x) = 1/2P(L^2 - x^2) \tag{13}$$

Assuming P causes a plastic hinge in this beam configuration, for the EP cross sections then Eqs. (12) and (13) must be equated to obtain:

$$2/3\sqrt{3}kB(3H^2 - \zeta^2) = 1/2P(L^2 - x^2) \tag{14}$$

Eq. (14) may be rewritten as a function of a new parameter ρ that represents the value of P for which the yield limit is reached:

$$\frac{1}{3}\left(\frac{\zeta}{H}\right)^2 - \rho\left(\frac{x}{A}\right)^2 = 1 - \rho \tag{15}$$

where $\rho = (P/P_0)(L/H)^2$ and $P_0 = 4\sqrt{3}kB$, which is the load for which the yield stress is first reached in the outer fibers.

For an EP cross section, ζ and ρ must satisfy the conditions $0 < \zeta < \mathrm{H}$ and $2/3 < \rho < 1$, respectively. The lower limit of ρ represents P for which the yield limit is reached at the outer fibers of the central cross section ($x = 0$). The upper limit represents P for which the plastic regions in the upper and lower portions of the beam join at the center. Fig. 5 shows the analytical function ζ and the numerically calculated EP frontiers of the plastic volumes considering a partial ($\rho = 0.8$) and a fully plastic ($\rho = 1.05$) cross section. Assuming ρ increases monotonically from zero, for $\rho < 2/3$ the beam behaves elastically, so its stress and strain fields are easy to determine. For $2/3 < \rho < 1$, part of the beam behaves plastically. Finally, for $\rho = 1$ the plastic regions in the upper and lower portions of the beam join at its central cross section $x = 0$ and the beam plastically collapses, becoming unable to carry larger loads.

To determine the deflections w of the beam, first consider its portion $0 \leq x \leq \mathrm{L}$. Using $\sigma = k\sqrt{3}$ when $y = \zeta$ into Eq. (8) for the central

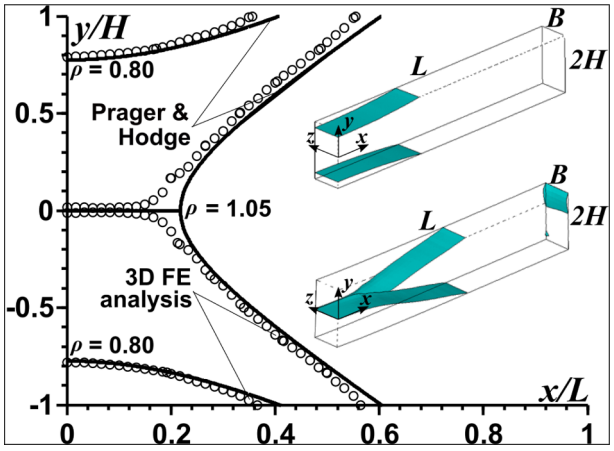

Fig. 5. Elastoplastic frontier for a partial (ρ = 0.8) and a fully plastic (ρ = 1.05) cross section.

portion, and combining Eq. (12) for an entirely elastic cross section and Eq. (13) for the fully elastic end portions of the beam:

$$\begin{cases} \frac{d^2w}{dx^2} = -\frac{k\sqrt{3}}{E\zeta} & \text{for the central portion} \\ \frac{d^2w}{dx^2} = -\frac{3}{8}\frac{P(L^2-x^2)}{EBH^3} & \text{for the fully elastic portion} \end{cases} \tag{16}$$

Eq. (15) is then solved for ζ and its result replaced into Eq. (16) for the central beam portion. Then, integrating with respect to x knowing that $dw/dx = 0$ for $x = 0$ and performing some algebraic manipulation, the central deflection w_0 is given by:

$$w_0 = \frac{P_0L^2}{EBH}\cdot\left[\frac{1}{4\sqrt{3\rho}}\sinh^{-1}\left(\sqrt{\frac{3\rho-2}{3(1-\rho)}}\right) + \frac{\sqrt{1-\rho}}{4\sqrt{3}\rho} + \frac{2\rho^2-1}{8\rho} - \frac{3\rho+1}{12\rho}\sqrt{\frac{\rho(3\rho-2)}{3}}\right] \tag{17}$$

Fig. 6 shows the changes in the normalized central deflection (w_0/w_0^*) as the normalized load $\rho = (P/P_0)(L/H)^2$ increases, where w_0^* given by Eq. (18) is the deflection of the central cross section of the beam at the instant when the yield stress is first reached in its outer fibers. The w_0/w_0^* ratio remains below 2 as long as ρ remains smaller than 95% of the load that causes yielding throughout the central cross section. Further details on this analytical solution can be found elsewhere [23].

$$w_0^* = \frac{5}{48}\frac{P_0L^2}{EBH} \tag{18}$$

Finally, Fig. 7 shows the variations of the relative errors between the analytical, V_a, and numerical, V_n, plastic volumes as a function of the number of elements along B, considering a partial plastic cross section under ρ = 0.8. Numerical analyses reproduce better the analytical solutions when the smallest unit of volume treated in the *pz* is defined by the improved criterion $V_e/8$. The relative error between V_a and V_n is reduced from 35% to 6% using the new approach.

3.2. Numerical results from the literature

To validate the EP FE numerical analyses, a second comparison is made with two recent 3D FE results taken from the literature, for M(T) [16] and for C(T) [17] specimens. Table 2 summarizes the geometry and loading conditions of these specimens. These references used 3D SOLID185 and SOLID186 elements, and for a fair comparison, the same type of elements is adopted here for the corresponding sub-models that contain the *pz*. However, both global models, which require a less refined mesh, use larger 3D SOLID186 elements.

As noted in the previous section, an improvement in the calculation of *pz* volumes considers one eighth of the volume element ($V_e/8$) as the smallest unit of volume, which corresponds to each Gauss integration point. In all simulations of the cracked specimens, before analyzing any of the sub-models used in this work, a mesh convergence study was performed based on evaluations of the total volume (V_t) of the *pz* developed around the crack front for different mesh sizes. These studies also involve calculations of the EP work U_{EP} inside the *pz*s. Such convergence tests are performed using the sub-modeling procedures described in the previous section. For a local analysis of stress and strain fields near the crack tip, it is necessary to apply a denser mesh at least around the crack front, as already suggested in many studies [17,24,25].

Fig. 8 shows the shape and volume of only 1/4 of the *pz* on an M(T) specimen with 5 mm thickness for $K_I = 30$ MPa√m. In Ref. [16] the size of the *pz* is based on the FEs that reach Mises stresses higher than S_Y in one of its integration points. The same criterion to evaluate the volume of the *pz* was adopted here and a similar value for V_t (19.96 mm^3) was obtained.

Fig. 9 shows vertical displacement predictions at different levels around the crack front for a C(T) specimen with crack-to-width $a/W = 0.74$, width-to-thickness $W/B = 7.25$, and $B = 10$ mm, induced by $K_I = 17.82$ MPa√m, and compares them with displacements obtained from [17].

As explained above, SOLID185 linear and SOLID186 quadratic elements are used in these simulations. Fig. 10 shows the variation of the total *pz* volume V_t as a function of the number of elements along the modeled half-thickness B/2 for 3 different cases, where E_s is the element size. The first one reproduces the case adopted in [17], which uses linear elements and V_e as the criterion to calculate the V_t of the *pz*. The second case also uses linear elements but the $V_e/8$ criterion, while the third uses quadratic elements with the improved criterion $V_e/8$. For the first case, the V_t of the *pz* converges to 9.9 mm^3 after 35 elements along B/2, while second achieves $V_t = 9.1$ mm^3 after 30 elements. Finally, the last one achieves the same volume with only 15 elements.

To evaluate the numerical efficiency of the improved criterion used in this work, a comparison is performed between the latter two cases. The CPU time required to evaluate in the same microcomputer the sub-model with 79,135 nodes and 69,120 linear elements was 19 min12 s; on the other hand, the sub-model with 38,575 nodes and 8640 quadratic elements demands only 8min19s. Therefore, the sub-model with quadratic elements reaches the same result using only 43% of the CPU time to solve the sub-model with linear elements. In addition, when the V_e criterion is taken into account, the V_t of the *pz* results in conservative predictions. The same tendency was noted when the EP work U_{EP} was evaluated in the convergence analysis, see Fig. 11. As a result, 15 elements along B/2 and the $V_e/8$ improved criterion to estimate the V_t of the *pz* are used for further analyses. The numerical U_{EP} calculations are performed using Eq. (19), which represents the summation of the U_{EP} work over all Gauss integration points inside the *pz*:

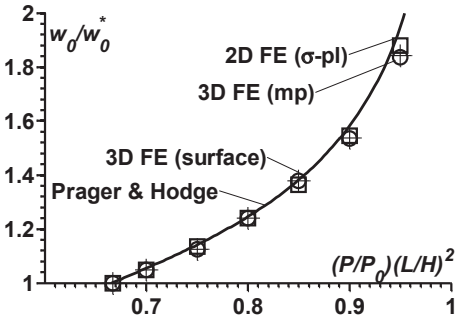

Fig. 6. Central deflection of an elastic-plastic beam.

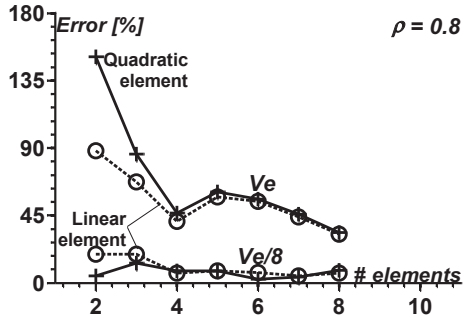

Fig. 7. Errors between the analytical V_a and numerical V_n plastic volumes counting the entire volume of the element V_e and its fraction $V_e/8$ in the pz volume for a partially yielded cross section under ρ = 0.8.

$$U_{EP} = V_e/8 \cdot \sum_{i}^{8n} u_{ep} \tag{19}$$

where n is the number of elements inside the pz, V_e is the element volume and u_{ep} is the elastoplastic work density in each Gauss integration point.

3.3. Experimental results

The specimens used in the present work are cut from an API 5L X80 steel plate with 21.85 mm thickness. Its tensile properties are measured by ASTM E8/E8M [26] standard procedures, using three sub-sized plate specimens cut along the thickness in both transversal and longitudinal directions of the plate. The average properties resulting from such tensile tests are listed in Table 3.

H and h are the Ramberg-Osgood parameters, using the engineering notation $\varepsilon = \sigma/E + (\sigma/H)^{1/h}$ [2]. For the toughness measurements, two SE(B) specimens 205 mm long, with width W = 44.3 mm and thickness B = 20.9 mm, are waterjet cut in a way that the crack would propagate on the transversal direction of the plate. Ultra-narrow notches with 20 mm depth from the surface are machined on a wire-cut electric discharge machine (EDM) to locate the crack at the middle of the SE(B). All the specimen dimensions are selected according to the ASTM E1820 standard [3]. The pre-crack length-to-specimen width ratio a/W = 0.55 chosen for the tests is in the middle of the range allowed by the standard, so the target pre-crack size is 4.4 mm. During the fatigue cracking procedure, both specimens are subjected to three-point bending under force control, with P_{max} equal to 0.9 of the maximum allowed force and $R = P_{max}/P_{min}$ = 0.1 under a frequency of 25 Hz.

After 83,523 cycles, the SE(B)-1 developed a surface crack size of 4.04 mm, while the SE(B)-2 resulted in a 4.20 mm crack after 92,452 cycles. Crack sizes are measured using a traveling microscope. After fatigue pre-cracking, V-shaped side grooves with a depth of $B/10$ are machined on both surfaces of the specimens (see Fig. 2). The E1820 standard recommends this operation because it avoids crack tunneling and shear lips, besides ensuring a plane-strain state and a straighter crack front during the test. The resulting net thickness B_N and the 45° V-notch root radius ρ of the grooved specimens are 16.72 mm and 0.5 mm, respectively.

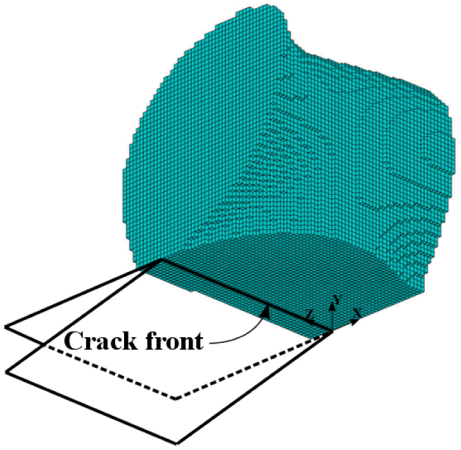

Fig. 8. Shape and volume of 1/4 of the pz developed around the crack front on an M(T) specimen for K_I = 30 MPa√m.

During the loading of the SE(B) specimens, their crack opening displacement (COD) and/or load-line displacement (LLD) are continuously measured to obtain their J-R curves. The partial unloading compliance methodisused for such J-R tests, controlled by the LLD with a speed of 0.003 mm/min. The first unloading/reloading point starts when the force reaches the expected $0.75 \cdot P_{max}$, and like all other measurements include three unloading/reloading sequences. The consecutive unloading/reloading points are chosen at COD intervals of 0.1 mm, and three unloading/reloading sequences are applied on the first 10 points. The force range in each point is $0.25 \cdot P_{max}$, such that it could provide enough data points after the material relaxation. It is worth noting that the specimens suffered a relaxation of almost 1kN in every point after the plastic deformation. Thus, waiting 30 s for the relaxation in each point was necessary. According to the E1820 standard, the compliance must be measured at each unloading/reloading point to estimate the crack size. The J-R curve is obtained from the assessed J and the crack extension Δa between the compliance points.

The displacement field on the specimen surface is simultaneously measured using a Correlated Solutions DIC (VIC-3D) system [27]. The device includes two 5-MP Point Grey GRAS-50S5M CCD digital cameras with a Tamron SP AF180mm F/3.5 lens attached to each camera, an adjustable fiber-optic light source, standard calibration grids, a data acquisition system, and suitable software to analyze the data. The digital cameras are mounted on an adjustable tripod in front of the specimen. The complete experimental setup is shown in Fig. 12.

It is not possible to determine the entire fracture resistance curve of this API 5L X80 steel by standard procedures, since it is too tough and its J-R curve grows higher than the *Jlimit* defined by the E1820 standard. Thus, only the crack tearing initiation toughness J_{IC} is evaluated from the intersection of the start of its J-R curve with a 0.2 mm offset line, see Fig. 13.

These initial J-R curves are also compared with those obtained in [28], which studied a high strength pipeline steel that also obeys the

Table 2
Cases published in the literature [16,17].

Specimen	a/W (–)	a (mm)	W (mm)	W/B (–)	P (kN)	K_I (MPa√m)	$\sigma n/SY$ (%)
M(T) [16]	0.25	20.00	80.00	16.00	92.14	30.00	33.00
				40.00	36.86		
				16.00	61.43	20.00	22.00
				40.00	24.57		
C(T) [17]	0.74	54.00	72.50	12.08	1.49	25.00	80.50
				24.17	0.75		
				7.25	1.77	17.82	57.38

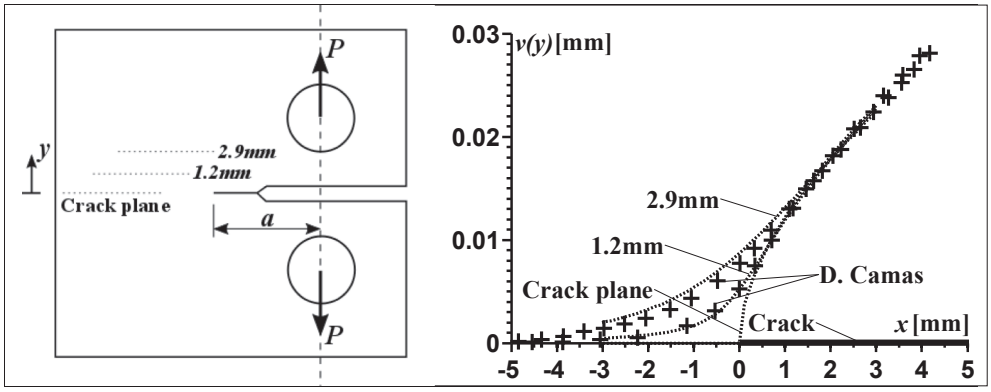

Fig. 9. Numerical vertical displacements on a C(T) specimen on its crack plane and at 1.20 mm and 2.90 mm from it, induced by a SIF K_I = 17.82 MPa√m.

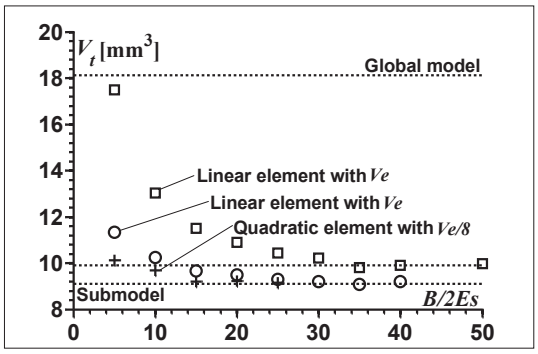

Fig. 10. Analysis of the V_t of pz for three different cases.

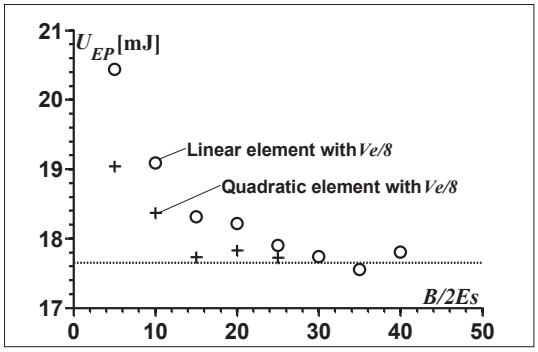

Fig. 11. Analysis of the EP work (U_{EP}) inside the pz for cases with the V_e/8 improved criterion.

Table 3
Tensile average properties of the studied API 5L X80 steel.

Orientation	E (GPa)	S_Y (MPa)	S_U (MPa)	H (MPa)	h (–)
Transversal	210	546	627	954	0.139
Longitudinal	210	527	612	946	0.148

API 5L X80 standard, alternatively named N550. All SE(B) samples are cut froma 48 × ½″ pipe section. The evaluated ratios a/W are 0.24 and 0.64, which represent a shallow and a deep crack, respectively, to characterize different constraints along the crack front. All specimens are machined with W = 23 mm, B = 11.5 mm and B/W = 2. To achieve plane-strain conditions recommended by the standard, 20% side-grooves are used, so B_N = 9.2 mm. The V-notch root radius (ρ) and angle (α) are not described in the reference. The tensile properties are measured at room temperature using specimens oriented in the pipeline longitudinal direction. The measured mechanical properties are

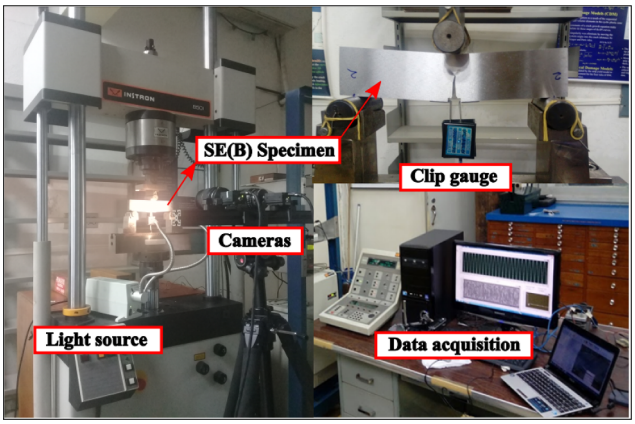

Fig. 12. Experimental setup used to measure the *J-R* curves and displacement fields on the specimen surface using the VIC-3D system.

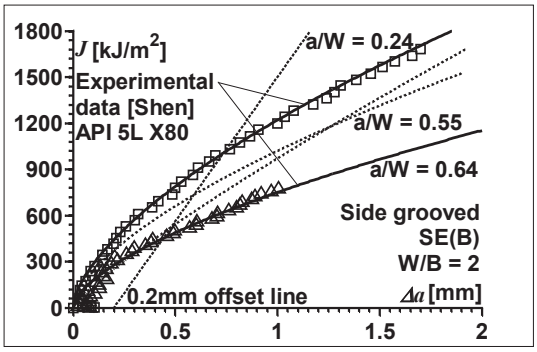

Fig. 13. Measured *J-R* curves.

S_Y = 570 MPa, S_U = 675 MPa, E = 207 GPa, and ν = 0.3, elongation ε_U = 0.422 and reduction in area RA = 0.683. From the experimental true σ-ε curve the Ramberg-Osgood parameters are determined: H = 892 MPa and h = 0.08.

Finally, the measured horizontal and transversal x-y plane displacements are compared with the results obtained from the 3D EP FE sub-model for an applied displacement, LLD = 8.55 mm. Figs. 14 and 15 show that the agreement between numerical (FE) and experimental (DIC) displacement results is quite good. For the horizontal displacements shown in Fig. 14, there is a change in slope near the crack tip region in both FE and DIC data. This gap is caused by the tunneling effect that often occurs during fatigue pre-cracks, as also noted elsewhere [17]. These discrepancies probably can be alleviated by modeling the actual curvature along the crack front. Transversal displacements (shown in Fig. 15) are reduced from approximately −0.36 mm at

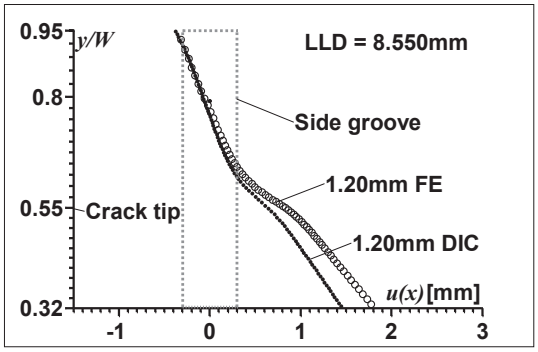

Fig. 14. Numerical (FE) and experimental (DIC) horizontal displacement ($u(X)$) fields at 1.2 mm from the crack plane for an applied displacement LLD = 8.55 mm.

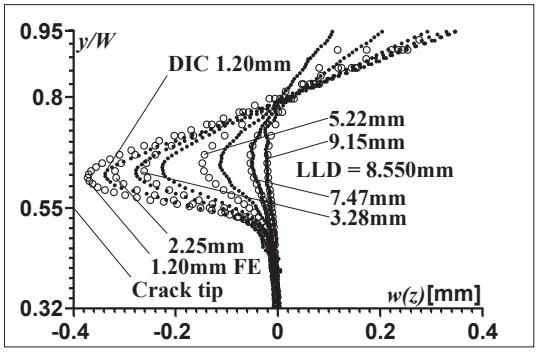

Fig. 15. Numerical (FE) and experimental (DIC) displacement ($w(z)$) fields in the transversal x-y plane at different distances (1.2 – side groove edge, 2.25, 3.28, 5.22, 7.47 and 9.15 mm) from the crack plane for an applied displacement LLD = 8.55 mm.

the side groove edge to an almost null value at 9.15 mm from the crack plane slightly ahead of the crack tip. The difference between FE and DIC results may be due to the same tunneling effect. It is also difficult to determine a reference point due to the impossibility of measuring displacements at free edges. Nevertheless, note that the differences between the FE and DIC results are relatively small.

4. Numerical results for two differently constrained specimens

For C(T) and SE(T) specimens loaded under a SIF K_I = 30 MPa√m, Fig. 16 shows how much the volume of the *pz* ahead of the crack front can vary for a given nominal driving force. Indeed, a quite remarkable difference in this volume can be seen through a comparison between two cases: an SE(T) specimen with geometry and loading ratios $W/B = 4$, $a/W = 0.6$, and $\sigma_n/S_Y = 0.2$, and a C(T) specimen with $W/B = 4$, $a/W = 0.4$, and $\sigma_n/S_Y = 0.8$, both loaded by the very same K_I. A very significant and most certainly non-negligible factor of 4 is observed between them! Notice that these simulations are run for specimens without side grooves, i.e., with $B_N = B$.

Overall, the same trend is noted when the *EP* work inside the *pz* is evaluated (see Fig. 17). However, the factor decreases to 1.9, which still is a very large difference. Hence, based on the physically appealing EP work arguments inside the *pz* around the crack front, it is possible to argue that the measured toughness values *JIC* should also dramatically change in those specimens.

5. Numerical validation through experimental toughness ratios

The objective of this section – and probably the main contribution of this work as well – is to validate the 3D EP FE calculations proposed here to model the *pz* sizes and shapes, as well as the plastic work U_{PL} spent inside them, through suitable experimental results. For this purpose, a comparison is made using the ratio of fracture toughness measured at the threshold of crack tearing for different constraint levels, e.g. $J_{IC,\sigma\text{-}pl}/J_{IC,\varepsilon\text{-}pl}$ [28] or $\delta_{IC,\sigma\text{-}pl}/\delta_{IC,\varepsilon\text{-}pl}$ [29]. The comparison is made through the ratio of the values of plastic work per *pz* volumes developed around crack fronts. They are also evaluated in both *σ-pl* and *ε-pl* conditions, e.g. $(U_{PL}/V_t)_{,\sigma\text{-}pl}/(U_{PL}/V_t)_{,\varepsilon\text{-}pl}$, as listed in Table 5.

There is no information about the exact loads that generated J_{IC} for the SE(B) specimens from Ref. [28] analyzed in Section 3.3. Hence, a new reference study is used here for such comparison purposes [29], which used a slightly higher strength pipeline steel API X90 to investigate thickness effects on the critical crack tip opening displacement δ_{IC} of SE(T) specimens. All tested specimens were cut longitudinally from a large pipe sample with nominal outer diameter 1013 mm and thickness 31 mm. From all available results, two B/W ratios are chosen for the following evaluation. The first one with $B/W = 0.5$ and a relatively low transversal constraint (*σ-pl* condition), whereas the second with $B/W = 6$ and a relatively high transversal constraint (*ε-pl* condition). All specimens are machined with W = 18 mm, $H/W = 10$ mm and $a/W = 0.4$. In addition, 15% side-grooves with a 0.5 mm root radius and an angle 45° are used to guide the crack.

The tensile properties of the API X90 steel are measured at room temperature (around 20 °C). Its main mechanical properties are S_Y = 640 MPa and S_U = 792 MPa. Young's modulus (E) and Poisson's coefficient (ν) are not described in Yizhe's paper. For both simulated cases these parameters are assumed E = 210GPa and $\nu = 0.3$. The true stress-strain curve used in the 3D EP FE models is shown in Fig. 18.

The critical CTOD δ_{IC} is defined from the intersection point of the resistance curve and the 0.2 mm blunting offset line, as illustrated in Fig. 19. It was noted a factor of 2.12 between $\delta_{IC,0.5}$ and $\delta_{IC,6}$ when determined by the double-clip gage method [29,30].

The measurements for the *pz* radius-to-specimen thickness ratio $S_r = r_{pz}/B$ are in good agreement with the constraint parameter S_r predicted for plane strain (ε-pl) at $\theta = 90°$, see Eq. (20). The critical load P_{IC} can be calculated from $K_I = [P_{IC}/\sqrt{(B{\cdot}B_N{\cdot}W)}]{\cdot}f(a/W)_{SET}$, where f $(a/W)_{SET}$ is given by Eq. (21) [31]. Table 4 shows the geometric parameters and loads used in the 3D EP FE models.

$$S_r = \frac{K_I^2}{4B\pi\sigma_Y}\left[\frac{3}{2}\sin^2\theta + (1-2\nu)^2(1+\cos\theta)\right] \tag{20}$$

$$f\left(\frac{a}{W}\right)_{SET} = 0.2832 + 3.8497\left(\frac{a}{W}\right) - 1.4885\left(\frac{a}{W}\right)^2 + 4.1716\left(\frac{a}{W}\right)^3 + 9.9094\left(\frac{a}{W}\right)^4 - 7.4188\left(\frac{a}{W}\right)^5 \tag{21}$$

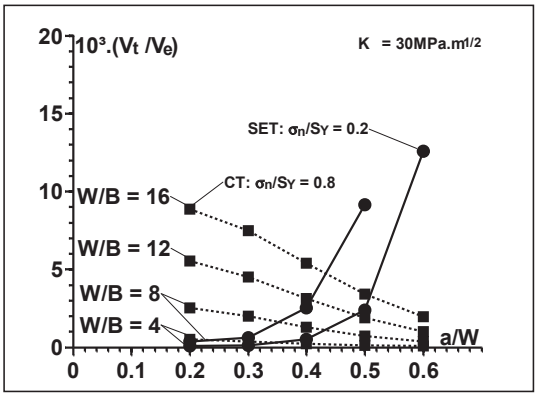

Fig. 16. Total *pz* volumes ahead of the crack front for several simulated cases.

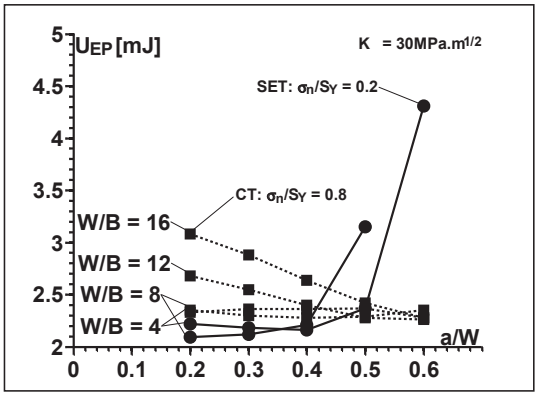

Fig. 17. EP work inside the total *pz* volumes for several simulated cases.

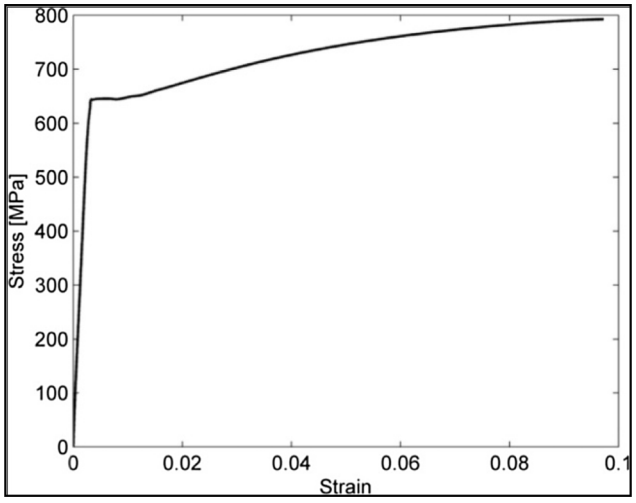

Fig. 18. The true stress-strain curve of the studied API X90 steel.

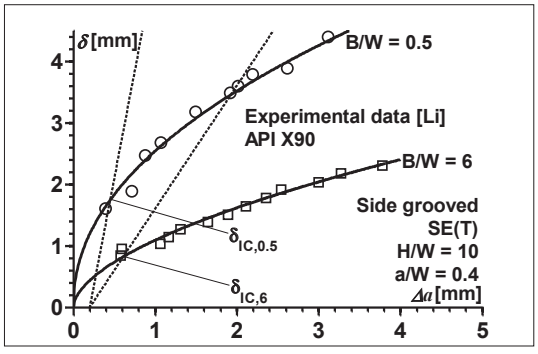

Fig. 19. Resistance curves and the δ_{IC} at crack initiation for different thickness specimens B/W.

Table 4
Geometry and load conditions for two cases [29].

δ_{IC} (mm)	a/W (–)	B/W (–)	S_r, ε-pl,$\theta = 90°$ (–)	K_I (MPa√m)	P_{IC} (kN)
1.745	0.41	0.5	0.418	108	57
0.823	0.39	6	0.040	116	787

Table 5
Numerical plastic work per *pz* volume (U_{PL}/V_t) and experimental critical CTOD δ_{IC} for each σ-*pl* and ε-*pl* conditions and their ratios.

B/W (–)	V_t (mm^3)	U_{PL} (mJ)	U_{PL}/V_t (mJ/ mm^3)	δ_{IC} (mm)
0.5	9.55	17.58	1.84	1.745
6	187.80	201.87	1.07	0.823
Ratio	–	–	**1.75**	**2.12**

All numerical and experimental data are listed in Table 5. The comparison between numerical prediction $(U_{PL}/V_t)_{,0.5}/(U_{PL}/V_t)_{,6}$ ratio and experimental data ratio $\delta_{IC,0.5}/\delta_{IC,6}$ using the double-clip gage method indicate quite good correlations. The gap between the ratios is caused by the tunneling effect that often occurs during fatigue pre-cracks, as noted elsewhere [17]. Thus, these discrepancies probably can be alleviated modeling the actual curvature along the crack front. In addition, there is a difference in the δ_{IC} and its ratios values between the double-clip gauge method, used here to compare, and the other methods as well discussed in [29].

6. Conclusions

In this work three-dimensional elastoplastic finite element analyses have been used to generate numerical predictions of plastic zone volumes in an un-cracked beam. The numerical analyses reproduced well the analytical solutions. The relative error between numerical and classic analytical plastic zone volumes was only 6%. Numerical analyses reproduced better the analytical solutions when the smallest unit of volume treated in the plastic zone was defined by the improved criterion Ve/8.

Three-dimensional plastic zone estimations by using a elastoplastic sub-modeling FE technique were presented to evaluate plastic zone sizes and shapes in cracked specimens. The estimates obtained using this technique were validated through numerical and experimental results found in the literature. In addition, the methodology for calculating plastic zone volumes considering the $V_e/8$ improved criterion was verified by numerical simulations, where a minimum of 15 elements per modeled thickness $B/2$ were needed to reach convergence. The results obtained using the numerical model were validated through displacements measured on the surface of the specimen using 3D DIC techniques.

The comparison between numerical plastic work calculated inside the *pz* volume and experimental fracture toughness data was quite reasonable. The discrepancy observed between them was probably due to the simplified model that assumesstraight crack fronts. Thus, this robust parameter based on plastic zone volumes and the plastic work performed inside them has potential to be treated as a new engineering approach to estimate the resistance to crack tearing initiation in any kind of components. Although such calculations may require non-trivial numerical techniques, they can be quite useful especially in cracked components with low transversal constraints (e.g., in pipelines). This approach has shown potential to be a useful tool to replace unreliable combinations based on K or J and constraint parameters such as T-stress, A_2, Q, and T_z in most practical structural applications.

Acknowledgement

The authors would like to thank the Brazilian funding agency CAPES for the scholarships granted, and USIMINAS for supplying the material used in the tests.

Appendix A

```
! Language: Ansys Parametric Design Language (APDL)
! This macro calculate the fraction of the 3D plastic zone generated inside the EP beam
! Implemented by Luiz Fernando Nazare Marques

RHO = 0.8                                  ! The percentage of the cross section plastification [ ]
ELE_B = 3                                  ! Elements along half-thickness [ ]
L = 300                                    ! Half-length [mm]
H = 30                                     ! Half-height [mm]
B = 30                                     ! Half-thickness [mm]
E_S = B/ELE_B                              ! Element size [mm]
E = 210000                                 ! Young's modulus of elasticity [MPa]
SY = 300                                   ! Yielding strength [MPa]
NU = 0.3                                   ! Poisson's coefficient [ ]
P_0 = 4*B*SY                               ! Reference load [N/mm]
P = P_0*RHO*(H/L)**2                       ! Distributed load [N/mm]
/FILNAM,BENCHMARK_RHO_%RHO%                ! Filename
/PREP7                                     ! Pre-processing
ET,1,SOLID186                              ! 3D Quadratic element - Brick 20
ET,11,200,7                                ! 2D element
MP,EX,1,E
MP,NUXY,1,NU
TB,BKIN,1,1                                ! Material model
TBDATA,1,SY,0
BLC4,0,0,L,2*H                             ! 2D Geometry
AESIZE,ALL,E_S
TYPE,11
AMESH,ALL                                  ! 3D Mesh
ALLSEL
VEXT,ALL, 0,0,B                            ! 3D Geometry
TYPE,1
EXTOPT,ESIZE,B/E_S,1
EXTOPT,ACLEAR,1
ALLSEL,ALL
VSWEEP,1,1,2                               ! 3D Mesh
ALLSEL
NSEL,S,LOC,Z,0
D,ALL,UZ                                   ! Symmetry about the x-y plane
ALLSEL
NSEL,S,LOC,X,0
D,ALL,UX                                   ! Symmetry about the z-y plane
ALLSEL
NSEL,S,LOC,X,L
D,ALL,UY                                   ! Constrained y axis displacement
ALLSEL
ASEL,S,AREA,5
SFA,ALL,PRES,P/B/2                         ! Distributed load
ALLSEL
/SOLU                                      ! Solution
ANTYPE,0
NLGEOM,1
NSUBST,500,10000,1
OUTRES,ERASE
OUTRES,ALL,ALL
LNSRCH,1
NEQIT,1000
PSTRES,1
TIME,1
ERESX,NO
SOLVE                                      ! Solution
/CTYPE,1
/EDGE,1,1
/CVAL,SY/E
FINISH
/POST1                                     ! Post-processing
PLNSOL,EPTO,EQV                            ! Plastified cross section
```

References

[1] ASTM E399-12, Standard Test Method for Linear-Elastic Plane-Strain Fracture Toughness K_{IC} of Metallic Materials, American Society for Testing and Materials, 2018.

[2] J.T.P. Castro, M.A. Meggiolaro, Fatigue Design Techniques vol. 3, CreateSpace, 2016.

[3] ASTM E1820-17a, Standard Test Method for Measurement of Fracture Toughness, American Society for Testing and Materials, 2018.

[4] C. Betegon, J.W. Hancock, Two-parameter characterization of elastic–plastic crack tip fields, J. Appl. Mech. 58 (1991) 104–113.

[5] N.P. O'Dowd, C.F. Shih, Family of crack-tip fields characterized by a triaxiality parameter – I, structure of fields, J. Mech. Phys. Solids 39 (1991) 989–1015.

[6] Z.Z. Du, J.W. Hancock, The effect of non-singular stresses on crack tip constraint, J. Mech. Phys. Solids 39 (1991) 555–567.

[7] T. Nakamura, D.M. Parks, Determination of elastic T-stress along three-dimensional crack fronts using an interaction integral, Int. J. Solids Struct. 29 (1992) 1597–1611.

[8] Y.Y. Wang, D.M. Parks, Evaluation of the elastic T-stress in surface cracked plates

using the line-spring method, Int. J. Fract. 56 (1992) 25–40.
[9] J.W. Hancock, W.G. Reuter, D.M. Parks, Constraint and toughness parameterized by T, ASTM STP 1171 (1993) 21–40.
[10] W. Guo, Elastoplastic three dimensional crack border field I. Singular structure of the field, Eng. Fract. Mech. 46 (1993) 93–104.
[11] W. Guo, Elastoplastic three dimensional crack border field II. Asymptotic solution for the field, Eng. Fract. Mech. 46 (1993) 105–113.
[12] W. Guo, Elastoplastic three dimensional crack border field III. Fracture parameters, Eng. Fract. Mech. 51 (1995) 51–71.
[13] C.S. Chen, R. Krause, R.G. Pettit, L. Banks-Sills, A.R. Ingraffea, Numerical assessment of T-stress computation using a p-version finite element method, Int. J. Fract. 107 (2001) 177–199.
[14] R.A. Souza, J.T.P. Castro, A.A.O. Lopes, L.F. Martha, On improved crack tip plastic zone estimates based on T-stress and on complete stress fields, Fatigue Fract. Eng. Mater. Struct. 36 (2013) 25–38.
[15] C. She, W. Guo, The out-of-plane constraint of mixed-modecracks in thin elastic plates, Int. J. Solids Struct. 44 (2007) 3021–3034.
[16] M. Besel, E. Breitbarth, Advanced analysis of crack tip plastic zone under cyclic loading, Int. J. Fatigue 93 (2016) 92–108.
[17] D. Camas, J. Garcia-Manrique, A. Gonzalez-Herrera, Numerical study of the thickness transition in bi-dimensional specimen cracks, Int. J. Fatigue 33 (2011) 921–928.
[18] D. Camas, et al., Numerical and experimental study of the plastic zone in cracked specimens, Eng. Fract. Mech. 185 (2017) 20–32.
[19] F. Yusof, Three-dimensional assessments of crack tip constraint, Theor. Appl. Fract. Mech. (2019), https://doi.org/10.1016/j.tafmec.2019.01.025.
[20] Y.G. Matvienko, G.P. Nikishkov, Two-parameter J-A concept in connection with crack-tip constraint, Theor. Appl. Fract. Mech. 92 (2017) 306–317.
[21] T. Kawabata, et al., Investigation on η and m factors for J integral in SE(B) specimens, Theor. Appl. Fract. Mech. 97 (2018) 224–235.
[22] D. Sen, J. Chattopadhyay, New η-factor equation for evaluation of J-integral of shallow cracked CT specimen considering R-O material strain hardening, Theor. Appl. Fract. Mech. 97 (2018) 98–107.
[23] W. Prager, P.G. Hodge, Theory of Perfectly Plastic Solids, John Wiley & Sons, 1951.
[24] T.L. Anderson, R.H. Dodds, Specimen size requirements for fracture toughness testing in the transition region, J. Test Eval. 19 (1991) 123–134.
[25] M. Graba, J. Gatkiewick, Influence of crack tip model on results of the finite element method, J. Theor. Appl. Mech. 45 (2007) 225–237.
[26] ASTM E8/E8M-16a, Standard Test Method for Tension Testing of Metallic Materials, ASTM, 2018.
[27] VIC-3D 2010, Correlated Solution Inc., http://www.correlatedsolutions.com/.
[28] G. Shen, W.R. Tyson, A. Glover, D. Horsley, Constraint effects on pipeline toughness, Proc 4th Int Conf Pipeline Tech, vol. 2, 2004, pp. 703–720.
[29] L. Yizhe, G. Baoming, M. Corrado, D. Caiyan, W. Dongpo, Experimental investigation of out-of-plane constraint effect on fracture toughness of the SE(T) specimens, Int. J. Mech. Sci. 128–129 (2017) 644–651.
[30] P.L. Moore, H.G. Pisarski, Validation of methods to determine CTOD from SENT specimens, 22nd Int Ocean Polar Eng Conf, (2012).
[31] F.C. Moreira, G.H.B. Donato, Estimation procedures for J and CTOD fracture parameters experimental evaluation using homogeneous and mismatched clamped SE(T) specimens, ASME 2010 Pressure Vessels and Piping Division Conference, 2010, pp. 711–720.